



Deep learning accelerated prediction of the permeability of fibrous microstructures

Baris Caglar ^{a,*}, Guillaume Broggi ^b, Muhammad A. Ali ^c, Laurent Orgéas ^d, Véronique Michaud ^{b,*}

^a Aerospace Manufacturing Technologies, Faculty of Aerospace Engineering, Delft University of Technology, Kluyverweg 1, Delft 2629HS, Netherlands

^b Laboratory for Processing of Advanced Composites (LPAC), Institute of Materials (IMX), Ecole Polytechnique Fédérale de Lausanne (EPFL), Station 12, 1015 Lausanne, Switzerland

^c Department of Aerospace Engineering, Khalifa University of Science and Technology, Abu Dhabi, United Arab Emirates

^d Univ. Grenoble Alpes, CNRS, Grenoble INP, 3SR Lab, F-38000, Grenoble, France



ARTICLE INFO

Keywords:

- B. Permeability
- B. Microstructures
- C. Numerical analysis
- Deep Learning

ABSTRACT

Permeability of fibrous microstructures is a key material property for predicting the mold fill times and resin flow path during composite manufacturing. In this work, we report an efficient approach to predict the permeability of 3D microstructures from deep learning based permeability predictions of 2D cross-sections combined via a circuit analogy. After validating the network's predictions in 2D and extending it to 3D, we investigate its capabilities for handling images of various sizes obtained from virtual and real microstructures. More than 90% of 2D predictions is within $\pm 30\%$ of their counterparts obtained via flow simulations, similarly for 3D transverse permeability predictions, while in 3D case computational time is reduced from several thousands of seconds to less than 10 s. This work provides a robust and efficient framework for characterizing the permeability of fibrous microstructures and paves the way for extending this capability to estimate the permeability of fabric mesostructures.

1. Introduction

Typical reinforcements used for manufacturing fiber reinforced polymer composites (FRPC) are made of woven, braided or knitted yarns that contain thousands of individual fibers or filaments [1]. Fabric construction, yarn geometry and filament count have implications for the manufacturability [2,3] as well as the mechanical performance of FRPCs [4–6]. Permeability, or the hydraulic conductivity, of the pore network is a 3D tensor defined by the pore structure within the fabrics and is a key set of input parameters to flow simulations carried out during mold design in Liquid Composite Molding (LCM) processes to predict mold-filling times and to optimize the injection strategies [7–9].

Historically, permeability has been characterized experimentally [10–14] and many variants are reported for both in-plane and out-of-plane permeability characterization with different boundary conditions, relying on (un)steady flow conditions, or involving one, two or three dimensional flow [10,11,13,15]. Owing to the development of numerical techniques to represent the fabric structures and to simulate the flow within those, interest is growing to replace the laborious and

delicate permeability characterization experiments by physics-based numerical simulation [16–19]. However, this approach lacks the representation of the inherent variability such as yarn deformation, nesting etc., as well as the random distribution of fibers within yarns [20,21]. To overcome this limitation, an alternative route emerged based on collecting the micro- and meso-structural 3D geometric information via X-ray computed microtomography scans and performing flow simulations within those domains [22–26]. Despite the aforementioned advances, these simulations still require access to high computational power as they typically require hours even in highly parallelized systems [27]. On the other hand, analytical models provide straightforward solutions to estimate the permeability of textile reinforcements. These models range from simple models based on porosity of isotropic porous media, [28–32], to models that also take into account the flow direction with respect to the fiber orientation, either across or along the fibers as well as the tortuosity [33–38], with some of these being only applicable to transverse flow [39–42]. However these solutions remain typically limited in terms of dealing with ordered/disordered fibrous structures, as well as local variability in the microstructures, such as abruptly

* Corresponding authors.

E-mail addresses: b.caglar@tudelft.nl (B. Caglar), veronique.michaud@epfl.ch (V. Michaud).

changing fiber volume fraction due to highly compacted areas or resin rich zones.

Artificial neural networks (ANNs) provide powerful alternatives for prediction of permeability, among many other predictive capabilities, as they can consider local fiber distribution patterns and relate these to bulk permeability in a generalizable manner. ANNs are made of processing units which can discover and learn complex and meaningful patterns in a dataset through a trial-and-error procedure - in the case of supervised learning. Deep learning is a subclass of these machine learning techniques, named from the presence of many processing units - also called layers - in series and in parallel in the artificial neural network [43]. In a broad sense, deep learning techniques have been exploited for many purposes such as speech recognition, language processing, autonomous-driving, medical diagnosis as well as in materials science [44–48]. Convolutional neural networks (CNNs) are a type of deep learning algorithm that takes images as input and relates the features of the image to a property of interest. In materials science, they have been used for predicting the thermal, mechanical and hydraulic properties, design and topology optimization of material systems [49–56]. In recent years, several studies explored CNNs suitability for predicting local flow fields and the permeability of porous media, mainly for isotropic porous media such as found in soil science [57–64]. To the best of our knowledge, these advanced techniques have not been applied to the study of oriented fibrous porous media and their particular highly anisotropic permeability.

In-line with the aforementioned works and to speed up the “learning phase”, the aim of this work is to propose a microstructure-guided upscaling procedure which combines (i) CNNs and (ii) analytical upscaling technique as a fast and accurate method to predict the permeability along the principal directions of fibrous 3D structures. The established route for this task involves providing the CNN with real 3D images of microstructures whose permeability is known, training the network for it to optimize its filters, and using the trained network to predict the permeability of previously unseen 3D microstructures. However, this would require extensive prior work to obtain the permeability and microstructure of hundreds to thousands of unique fiber arrangements. An alternative route involves the computer generation of 3D images, followed by fiber scale flow simulations to estimate the permeability, then training a 3D neural network on this set of generated images. Yet, this is still highly computationally intensive. To further increase the computational efficiency in case of highly oriented fibrous media exhibiting transverse isotropy, we propose to test the possibility of using a CNN that predicts the permeability values of 2D slices along the fiber direction of artificially generated 3D structures, and then to use an electric circuit analogy as a simple upscaling technique (which is well suited to the considered fibrous media only) to estimate the permeability of 3D structures based on individual slices’ permeability predicted by the neural network. This allows reducing the computational time from several thousands of seconds required for running 3D flow simulations to estimate the permeability to less than 10 s without sacrificing the permeability estimation quality, as will be discussed in the following sections. After validating the 2D and 3D permeability prediction accuracy of this highly efficient approach, we investigate image pre-processing strategies to demonstrate the suitability of our methodology in images that have a different size than what the neural network expects as input (*i.e.*, images with pixel dimensions different from 400 × 400 pixels as will be introduced in the following sections) or images with very large or very small fibers; or in other words, our approach is to use synthetic data to train a CNN with the aim to transfer learning to real microstructures where the image size as well as the fiber diameter can vary.

2. Methods

2.1. Elementary volume generation

Training and testing the suitability of a CNN for predicting the permeability requires generating many elementary volumes (EVs) that will form a large dataset with good coverage in terms of v_f , fiber radius r , fiber orientation and spatial distribution patterns. As discussed by Rimmel *et al.* [65], images containing on the order of hundreds of fibers where each fiber’s r is represented by approximately 10 pixels result in acceptable permeability values when the permeability of these images is estimated via solvers working directly on the images (*i.e.*, solvers that avoid using mesh based solvers thus bypassing a meshing procedure), as is our case. More specifically, the authors compared three cases with 262, 484 and 799 fibers and concluded that the case with lowest fiber count was more prone to probability of individual images whose permeability is estimated to be 0 due to locally blocked structures. As the computational cost of EV generation increases as the number of fibers increases; using larger images as input to CNNs implies larger downstream layers, further increases the computational cost.

Based on these considerations, we procedurally generated images of practically aligned fibers, with dimensions of 400 × 400 pixels where each pixel corresponds to area of 1 μm^2 and where the fibers had one of the following number of pixels as their radii, r : 6, 8, 10, 12, or 14 pixels and where the fiber content v_f varied between 0.25 and 0.70, by increments of 0.05. This resulted in microstructures whose number of fibers varied between 65 ($r = 14$ pixel, $v_f = 0.25$) and 990 ($r = 6$ pixel, $v_f = 0.70$), see Supporting Table 1 for the number of fibers in all the studied cases. We used a Monte-Carlo procedure similar to that summarized by Chen and Papathanasiou [66,67], which starts from an arbitrary packing of fibers with desired r and v_f and attempts to move fibers one by one in randomly selected directions at a random extent (see Supporting Fig. 1 for additional information). Despite the suitability of this approach to generate 2D microstructures, the sudden jumps of fibers result in an undesired short-range tortuosity as depicted in Fig. 1a. To overcome this limitation, we defined an initial direction for each fiber which is slowly and randomly changed at each new slice as visually depicted in Supporting Fig. 2. This allowed us to generate microstructures as shown in Fig. 1b which was made up of fibers which had a long-range tortuosity while avoiding sudden jumps between successive slices.

2.2. Flow simulations

When considering at the pore scale the Stokes flow of an incompressible Newtonian fluid, the macroscale flow through porous media is described by Darcy’s law:

$$\mathbf{u} = -\frac{1}{\mu} \mathbf{K} \cdot \nabla P \quad (1)$$

where \mathbf{u} is the volume averaged flow velocity, \mathbf{K} is the permeability tensor, μ is the resin viscosity and ∇P is the pressure gradient driving the resin impregnation through the pores. \mathbf{K} is a positive definite symmetric tensor which can be reduced to its diagonal form represented by K_x , K_y and K_z terms corresponding to permeability along the x -, y -, and z -directions when these directions are the principal directions of \mathbf{K} as it is the case in the simulations shown hereafter.

After generating the EVs, we performed flow simulations to extract the transverse and axial permeability values. We performed simulations on EVs with a depth (in y -direction) of one (*i.e.*, on 2D slices) to train the CNN as well as on full EVs (which consisted of 800 slices) to validate our approach based on combining both the circuit analogy as an upscaling technique which is well suited for the considered fibrous media and CNN predictions.

We opted for the Geodict software (Math2Market® GmbH) and its FlowDict module to perform our fiber scale simulations, as it can

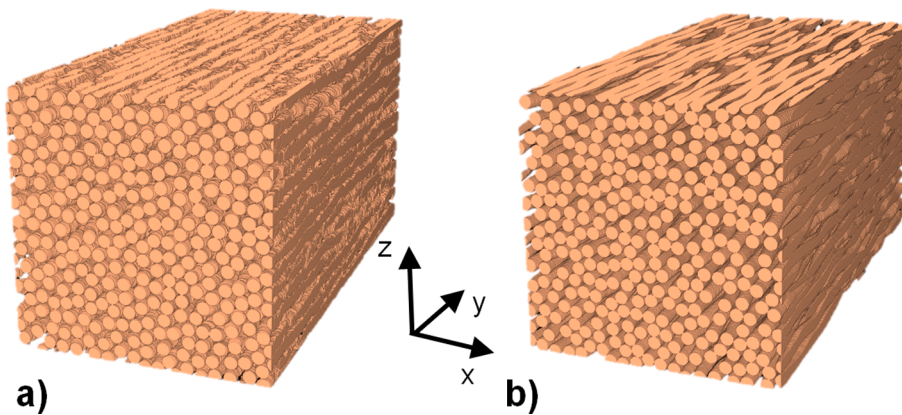


Fig. 1. a) EV generated by the original Monte-Carlo approach, b) EV generated without the short-range behavior. In both cases, $r = 10$ pixel, $v_f = 0.6$.

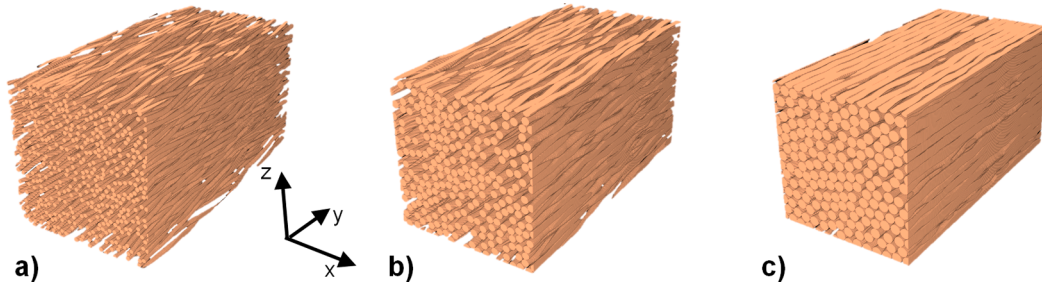


Fig. 2. Some examples of generated 3D architectures. a) $r = 6$ pixel, $v_f = 0.3$, b) $r = 10$ pixel, $v_f = 0.5$, c) $r = 14$ pixel, $v_f = 0.7$.

perform the simulations directly on the binarized images thus eliminating the need for mesh generation and as it can be automated via Python scripting to repeat the simulations on thousands of 2D binary images. We used an Explicit Jump-Stokes solver to solve the governing Stokes flow equations (*i.e.*, at negligible or zero-valued Reynolds number) as reported in earlier work for permeability characterization [22,65,68] with boundary conditions visually outlined in Fig. 3. More specifically, we defined periodic boundary conditions with implicit inlet and outlet along the flow direction (as shown in Fig. 3a for the x -direction) and defined periodic boundary conditions in the tangential directions as our EVs already had periodic boundaries as well as to minimize computational time without sacrificing the accuracy, as reported in [65] for similar simulations performed with the same software/module to extract transverse permeability of 2D microstructures. To run the simulations, the EVs were subjected to a macroscopic pressure difference of 0.02 Pa and the fluid viscosity was arbitrarily set to 1 mPa s.

2.3. CNN architecture

We implemented a modified version of AlexNet [69] architecture that is derived from LeNet network and paved the way for the most recent architectures which are based on the similar filter features. It provides fairly good results in both complex classification and regression tasks [70,71] and is available in Matlab's Deep Learning toolbox. The design of the CNN is outlined in Fig. 4a. CNN takes a matrix with a size of 400×400 (*i.e.*, an image with 400×400 pixels) and outputs the permeability, thus the network is set up for a regression task where the input is an image and the output is a numeric value. As mentioned before, we studied both axial and transverse permeability values and we used the same network architecture after training it with the desired data type. Each convolutional block shown in Fig. 4 consists of a convolutional layer followed by a rectified linear unit (ReLU) as the activation function which is then followed by batch normalization and max

pooling layers. The last convolutional block is followed by a dropout layer with a drop probability of 0.2 and by a fully connected layer to adapt the network to a regression task. The use of batch normalization and the dropout layer are common practice to avoid overfitting; batch normalization also accelerates the training process [72–74]. The filters (or kernels) in convolution layers have a size of 7×7 , 5×5 , and 3×3 respectively. All three convolutional layers' filters have a stride of 1 and paddings of 3, 2, and 1 and number of filters is 16, 32 and 64 respectively. Similarly, max pooling layers' size and stride vary with the first two of them having a size of 4×4 and a stride of 4 while the last one has a size of 2×2 and a stride of 1.

In total there are 50 unique microstructure types (5 different pixels per r and 10 different fiber content v_f), each with 1000 unique slices along the fiber direction. Out of these images, 1280 of them are selected randomly and used in the CNN training. As a 2D microstructure's permeability is identical when it is flipped upside down or left to right, we augmented the image input by flipping the images and used them during CNN training with a split of 3:1 between training and validation images.

On the neural network output side, we used the logarithm of permeability and mapped it between -1 and 1 using the minimum and maximum values. This approach outperformed other options during our early trials such as directly using the permeability or mapping with the mean and standard deviation of the logarithm of permeability. After defining the CNN architecture, pre-processing the input and the output data, we trained the CNN for 500 epochs using the ADAM optimizer via Matlab Deep Learning Toolbox (see Supporting Table 2 for the hyperparameters used in training) on an Nvidia Quadro RTX6000 with 24 GB memory; the training lasted approximately 14 h. Fig. 4b shows the evolution of root mean square error (RMSE) for training and validation data over 500 epochs. Stable value of RMSE for validation data indicates the absence of overfitting, a desired feature for any neural network training and fluctuation in the training curve is expected due to the use of a dropout layer [75].

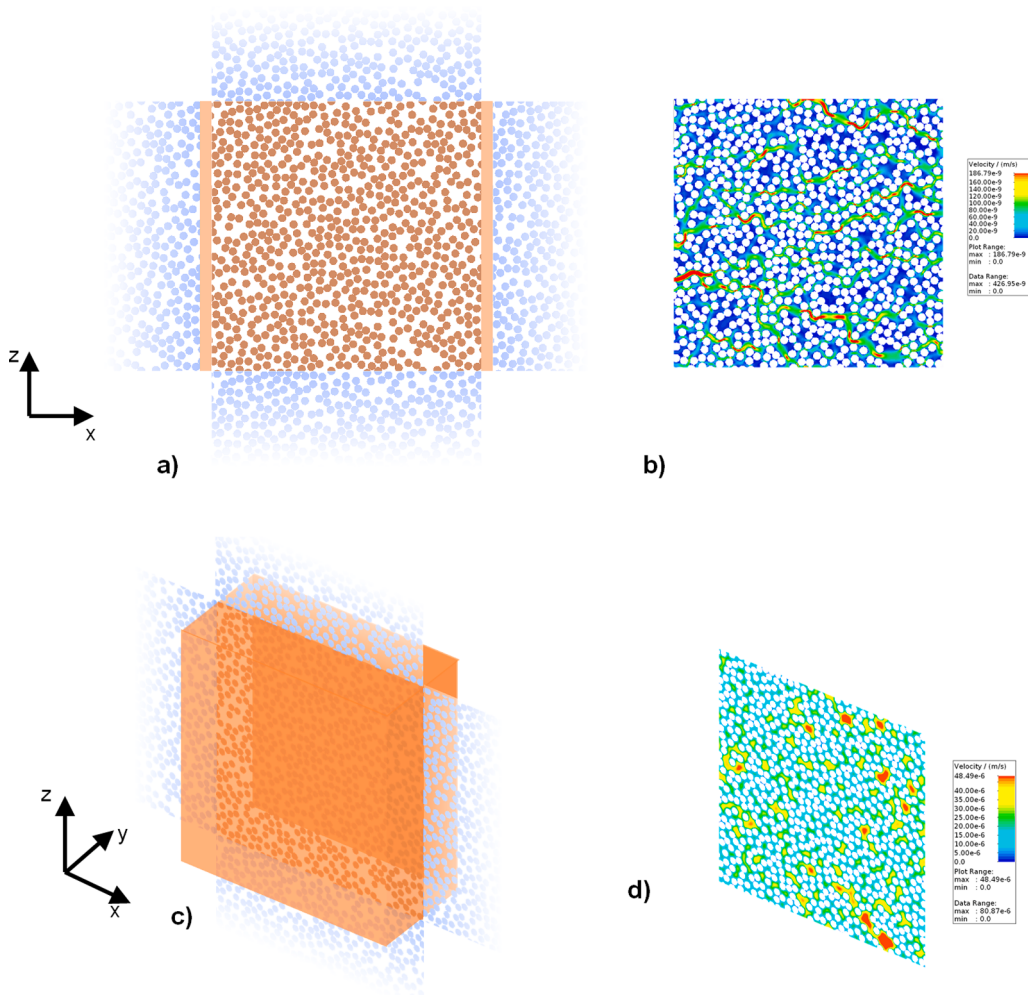


Fig. 3. Boundary conditions and corresponding flow fields in x- and y-directions (velocity magnitude), respectively. (a&c) Boundary conditions highlighting the implicit inlet/outlet voxels in orange and periodic tangential boundaries in blue. (b&d) velocity magnitude fields for the microstructure and boundary conditions shown in a&c.

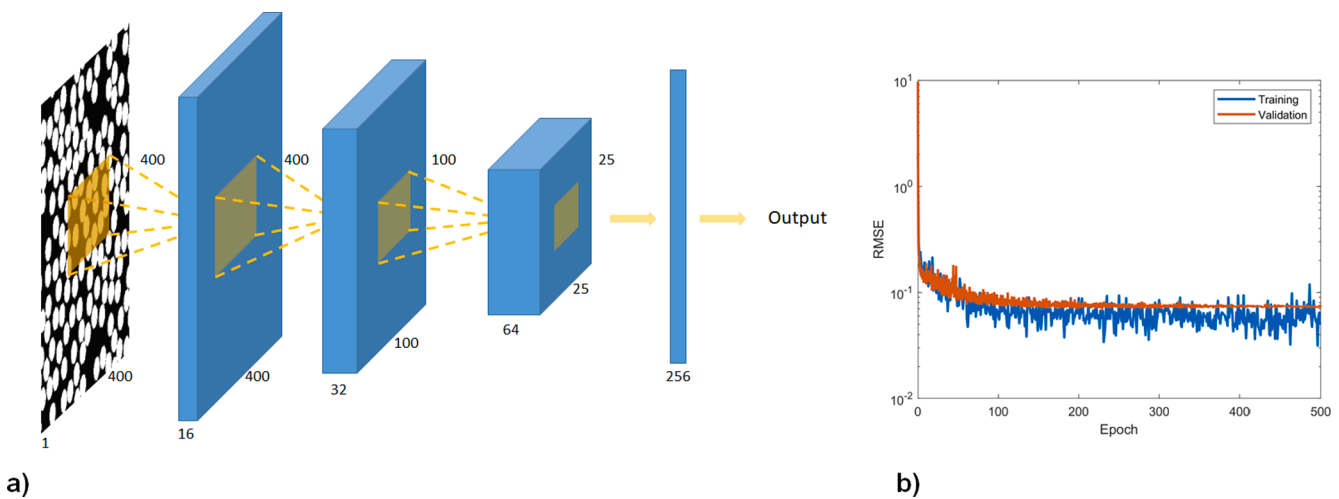


Fig. 4. a) CNN architecture used in this study. Each convolution block corresponds to a convolution layer followed by ReLU, batch normalization and max pooling layers. b) Evolution of root mean square error (RMSE) for training and validation parts of data.

3. Results and discussion

3.1. 2D transverse and axial permeability

We trained the CNN with the architecture shown in Fig. 4a for two different cases: (i) to predict the permeability along the x -direction, K_x , and (ii) to predict the permeability along the longitudinal y -direction, K_y respectively. It is also worth noting that the transverse directions (*i.e.*, x - and z -directions) can be tackled using a single network as the input 2D images can be transposed such that the neural network trained for K_x prediction can also be used for predicting K_z , as will be demonstrated below. Fig. 5a and b show, for x - and y -directions respectively, the neural network predictions and the corresponding simulation results for 3000 randomly selected images from the test data (see also Supporting Figs. 3 and 4 for the histograms of permeability results obtained via simulations and via the neural network predictions). In general, the predictions seem to be well-aligned with the simulation results for both directions. Even though the scatter is quite limited for the y -direction, predictions for x -direction deviate from the simulation results at low permeability values (roughly for permeability values lower than $1 \times 10^{-13} \text{ m}^2$ typically obtained when v_f was equal to or higher than 0.65). Coincidentally, Geodict tends to return 0 for transverse permeability of high v_f images and we excluded these data points from the training and testing of the neural network. This practice obviously results in an imbalance within the dataset. The so-called class imbalance is a common issue, and refers to the high representation of one of the classes in the data and the resulting bias in the learning process in favor of the dominant class [76,77]. We note that improving the balance would require more simulation results with very high v_f images. However, accounting for those cases would require switching to a mesh-based simulation approach where local mesh refinement between the narrowly spaced fibers would be necessary. For practical reasons, we opted to avoid switching to a mesh-based solver and used the dataset as is. This imbalance in the dataset might have contributed to the scatter in Fig. 5a that is more pronounced in the low permeability regime.

Considering the predictions in both directions, the deviation from the Geodict results seems to be rather low for all the images except those where fiber radius is 14 pixels, as will be quantified in the following paragraph. Considering that the 14 pixel radius case is less prone to discretization (or rasterization) based representation errors, that are prominent at low pixel per radius situations, we suspect that the relatively low performance for the 14 pixel radius case could be improved by altering the padding as well as the filter sizes. However, we note that a sensitivity study of the aforementioned parameters will not be carried

out in this first paper as each modification requires subsequent changes in the downstream layers of the network to maintain the output sizes; this will be investigated in a follow-up work.

To quantify the deviation of the CNN predictions from the simulation results, Fig. 6 reports the cumulative distribution of deviation in relative terms $|GD - NN|/GD$ where GD and NN correspond to Geodict results and neural network predictions, respectively (see also Supporting Fig. 5 for corresponding histograms). Dashed gray lines correspond to 30% deviation between the simulation results and the network predictions. The choice of 30% deviation might seem arbitrary at first glance. However, it corresponds to the deviation range found experimentally under strictly controlled characterization settings [11,12]. In general, the deviation is lower along the y -direction predictions in comparison to those along the x -direction; only the 14 pixel radius case stands out from the rest of the results with a slightly higher difference between simulation results and the neural network predictions. As mentioned above, this is suspected to originate from the mismatch between the characteristic feature size (boundaries of fibers which happen to have 14 pixels radius) and the filter sizes and padding settings as also reported in [63,78] and will be investigated in a future work. We also note that the relatively low fiber count in the images with 14 pixel radius fibers might have reduced the predictive capability of the neural network. With the same logic, the relatively low deviation for the 6 pixel radius case in Fig. 6 originates from the relationship between the pixel per radius and the filter sizes. The relatively higher scatter along the x -direction predictions manifests itself as $\sim 97\%$ of predictions (upper dashed gray line in Fig. 6a) having less than 30% deviation from the simulated results in the best case with 6 pixel radius. However, we note that even in the worst case, $\sim 90\%$ of the predictions (lower dashed gray line in Fig. 6a) are within the 30% deviation range, and the scattered points in Fig. 5a result in an extended upper tail for the 14 pixel case in Fig. 6a.

3.2. 3D permeability

3.2.1. Circuit analogy based on 2D predictions

In this section, we investigate the suitability of combining 2D permeability predictions *via* circuit analogy to estimate the 3D permeability of fibrous microstructures. To that end, we generated 15 new microstructures each consisting of 800 slices along the fiber direction with slices having a dimension of 400×400 pixels. Table 1 shows the fiber radii, r , and fiber content, v_f , of the studied microstructures and the runtimes of the Geodict flow simulations in all three directions.

For x - and z - directions, the equivalent permeability is calculated by the circuit analogy of 800 resistances ($1/K_x$) in parallel using the

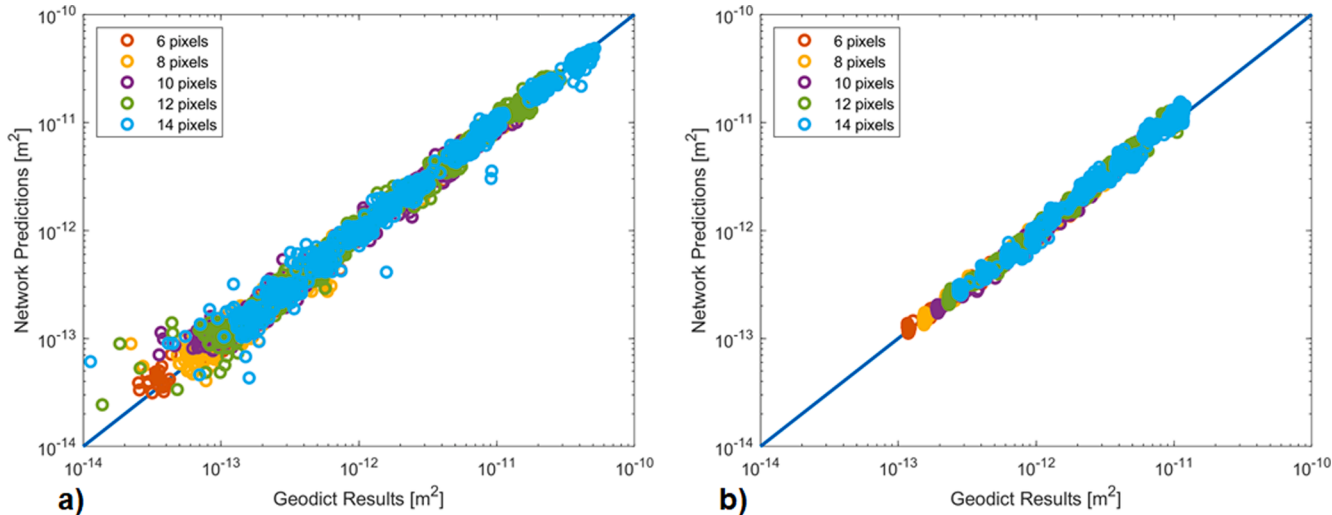


Fig. 5. Neural network predictions vs. Geodict results. Results along the x -direction (a) and the y -direction (b).

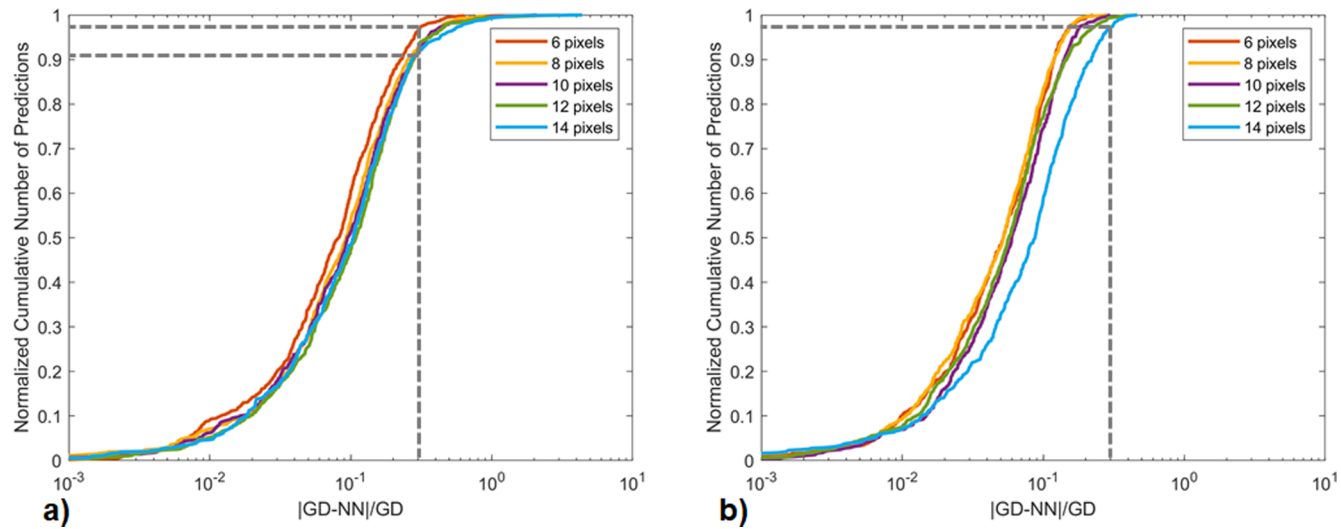


Fig. 6. Cumulative number of predictions as a function of the predictions' deviation from simulation results. Results along the x-direction (a) and the y-direction (b).

Table 1

Runtimes (in seconds) of 3D flow simulations in Geodict for the investigated microstructures with different v_f and pixel per radius and dimensions of $400 \times 400 \times 400$ pixels.

	v_f						
		0.3	0.4	0.5	0.6	0.7	
Fiber radius r [pixels]	6	X	3536	5234	7738	5943	5010
		Y	2653	2914	3291	3343	3661
		Z	2436	4653	4214	6000	8021
	10	X	1907	3140	4225	4932	5140
		Y	2191	2636	3201	3553	4096
		Z	2286	2736	4052	5602	5109
	14	X	1675	2500	2960	3858	4558
		Y	2066	2548	2126	2639	4921
		Z	1766	2336	2483	6978	8118

arithmetic mean of individual slices' permeability or in other words, a Voigt bound of the flow resistivity whereas along the y-direction case, the equivalent permeability is based on the circuit analogy of 800 resistances ($1/K_y$) in series using the harmonic mean of individual slices' permeability or, in other words, a Reuss bound of the flow resistivity.

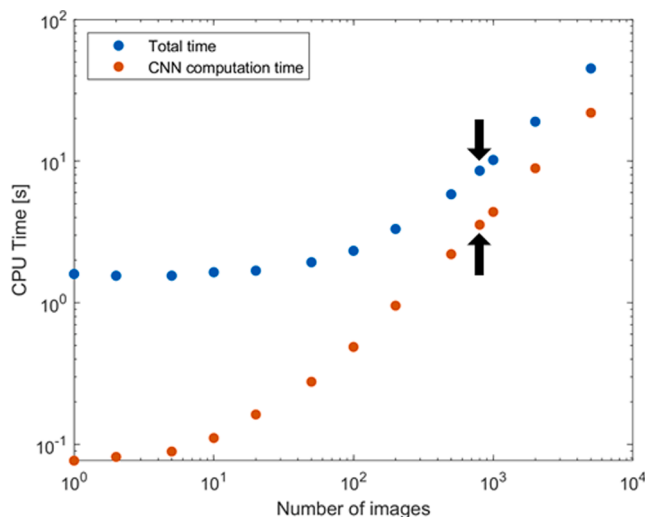


Fig. 7. Computational time required for permeability prediction using the CNN.

Fig. 7 shows the runtimes of the CNN based permeability prediction algorithm and for 800 images the total duration is 8.56 s (including the time spent for loading the network, loading the images and subsequent calculations for circuit analogy, see also Supporting Table 3 for a list of the computational times presented in Fig. 7). Compared to the simulation runtimes listed in Table 1 that are on the order of thousands of seconds, the merit of this approach in terms of reducing the computational intensity is clear and its prediction accuracy will be investigated in the following subsections.

Fig. 8 shows the construction of the circuit analogies and the reader is referred to our previous work for a detailed description of circuit analogy for permeability estimation purposes [2,79]. Fig. 9 shows the permeability values obtained via 3D simulations (GD-3D), the mean and the standard deviation of 2D permeability values obtained via Geodict (GD-2D) and the neural network (NN-2D) as well as the resulting circuit analogy results, namely GD-circuit and NN-circuit. Fig. 9a, b, and c report the results for $r = 10$ pixel cases for x-, y-, and z-directions, respectively, and the same results for $r = 6$ and 14 pixel cases are reported in Supporting Fig. 6. Results show a characteristic difference between the trends for x- and z-directions on one side, with most of the results falling in a small range. On the other side, along the y-direction, there seems to be an order of magnitude difference between 2D results and 3D results, both for the simulation and the circuit analogy.

Along the x- and z-directions, the circuit analogies (GD-circuit and NN-circuit) and 2D permeability results (GD-2D and NN-2D) exhibit a small scatter except for very high v_f cases where the high standard deviation of GD-2D results is due to simulation returning 0 for the permeability in these cases as reported in previous subsections. Fig. 9a and c show that the circuit analogy of neural network predictions (NN-circuit) approximates well the permeability obtained via the flow simulation on the full 3D geometry. Fig. 10a, b, c shows the ratio, $K_{NN\text{-circuit}}/K_{GD\text{-3D}}$, for the three studied radius value (6, 10, and 14 pixels per radius); the ratio fluctuates between ~ 0.6 and ~ 1.1 for the results along the x- and z-directions, with a general tendency of neural network circuit underestimating the permeability around a ratio of ~ 0.8 (see also Supporting Fig. 7 for $K_{GD\text{-circuit}}/K_{GD\text{-3D}}$ results). However, given the fact the 3D simulations take hours to run and there is an entry barrier to the use of any software, the value of the neural network circuit analogy lies in its accuracy as well the fact that one can obtain these results within a fraction of a second. Another interesting behavior is the departure of both GD-3D and NN-circuit from Gebart's permeability predictions (see ref. [33] or supplementary document for Gebart permeability models' equations for both longitudinal and transverse cases) at high v_f regime, a phenomenon also observed in Refs. [80,81].

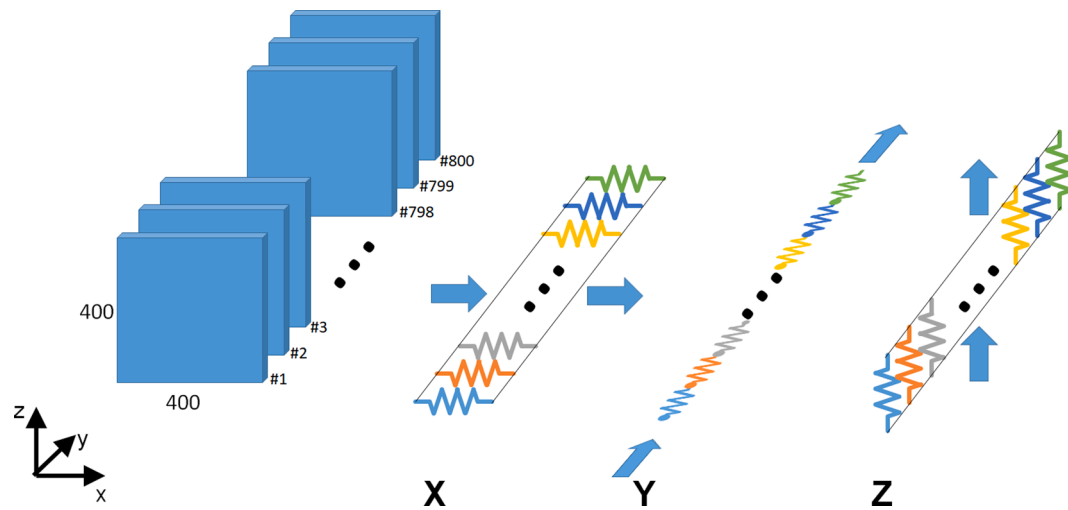


Fig. 8. Circuit analogy configuration used for estimating the principal permeability values of the considered 3D fibrous structures.

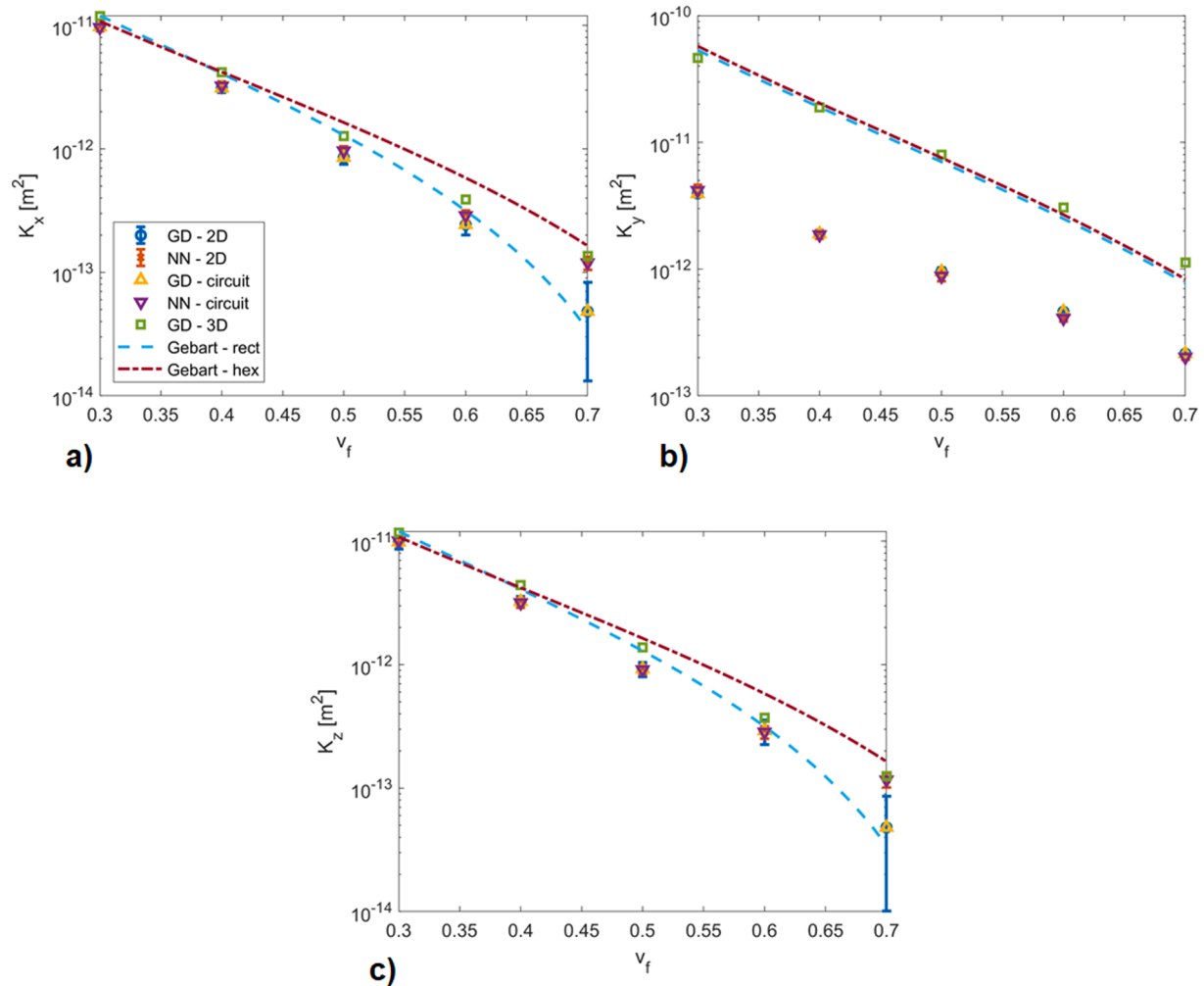


Fig. 9. Permeability results obtained via 2D, 3D simulations and circuit analogy of the neural network predictions, on images with $r = 10$ pixel. a, b, and c show the results along the x-, y-, and z-directions, respectively.

further validating our simulated and predicted transverse permeability results.

Implementing a slightly modified neural network that makes use of 3D images instead of 2D ones could be a route for increasing the

accuracy of the permeability predictions of 3D images. However, this would require hundreds if not thousands of unique 3D images and to perform the simulations on each 3D image so that they can be used for training, validating, and testing the neural network. It is not hard to

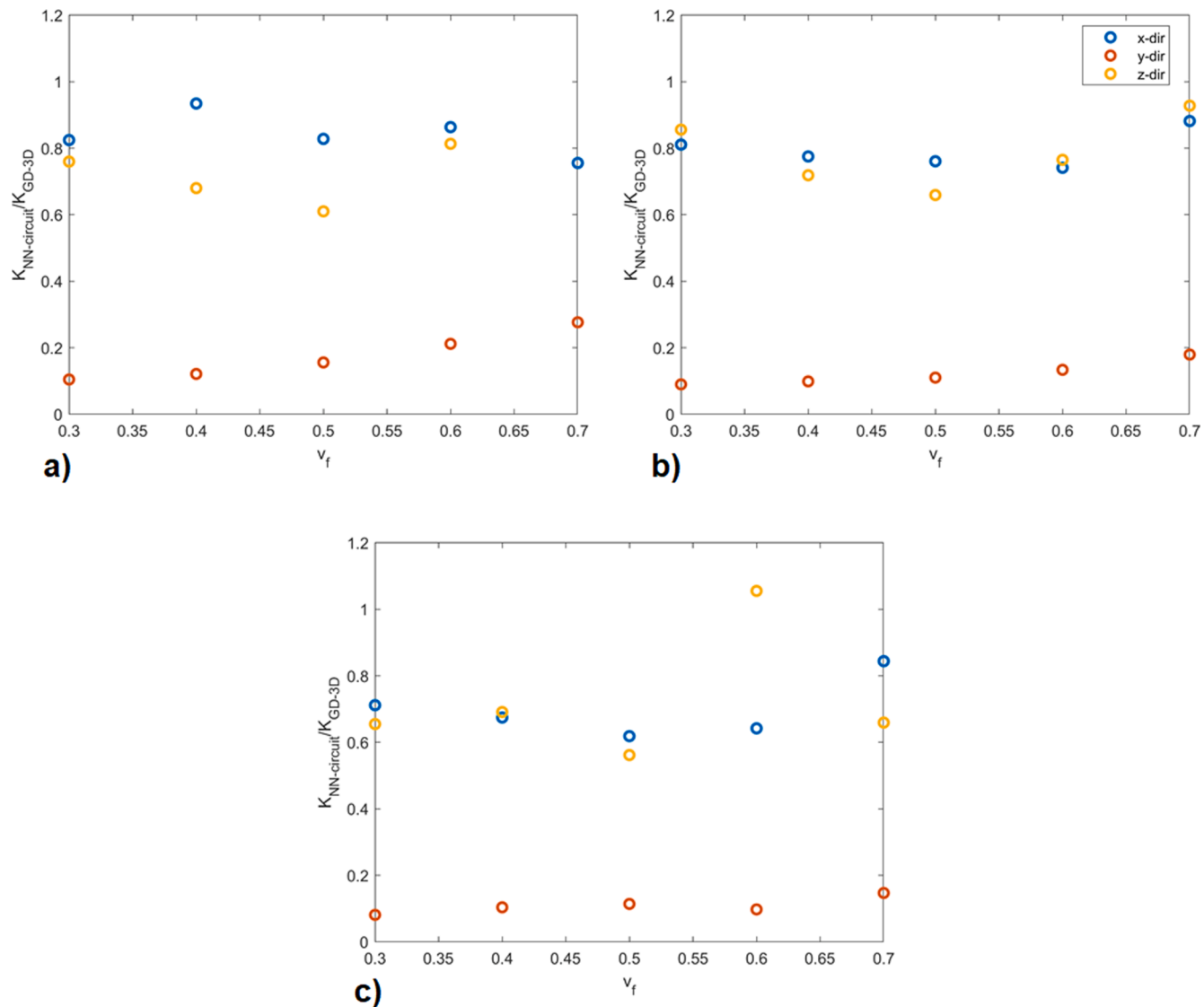


Fig. 10. Ratio between the circuit analogy results and the 3D simulation results ($K_{NN\text{-circuit}}/K_{GD\text{-3D}}$). a, b, and c show the results for the 6, 10, and 14 pixel per fiber radius cases respectively.

imagine that this task would require several months of computation, thus reiterates the value of our approach as it only relies on simulations on 2D images which take much shorter time to generate as well as to perform the flow simulations on these. We note that another approach to improve the accuracy in prediction of the 3D permeability tensor is to make use of more complex relations, such as an upscaling approach based on the tortuosity and specific surface area definition as pursued by Saxena *et al.* [82]. However, as demonstrated in that paper as well, the use of tortuosity and specific surface area usually implies lower permeability as one goes from 2D to 3D while 3D permeability is higher in our case. This inversed relationship might result from the simulation setup that we used (boundary conditions etc.), as also manifested along the y-direction results shown in Fig. 9b.

For the y-direction results, *i.e.*, along the main fiber orientation, there is almost an order of magnitude difference between 3D simulation results and the circuit analogy, as well as between 3D and 2D simulation results. Considering that the 3D simulation results are comparable with Gebart's permeability predictions and slightly higher than those at high v_f range as also reported by Endruweit *et al.* [80], and as the agreement between 2D simulation results and CNN predictions has been established in the previous section, the difference seems to be originating from the 2D simulation results and their circuit analogy. The agreement between

2D permeability predictions and 2D simulation results is already established in section 3.1, thus the issue originates from our 2D flow simulations as will be detailed in what follows. Upon closer inspection of the simulation settings, the implicit inlet/outlet definition stood out as a potential source of error. To investigate this, we took a random slice from every one of 15 studied configurations and extruded it to a depth of 10, 100 and 1000 slices as visualized in Fig. 11a, repeated the simulations and collected the permeability estimations. Fig. 11b shows the permeability predictions normalized with the permeability obtained with images of 1000 slice depth (K_i/K_{1000} where $i = 1, 10, 100, \text{ or } 1000$) for $r = 10$ pixel case and in Supporting Fig. 8a and c for $r = 6$ and $r = 14$ pixel cases. Supporting Table 4 presents the corresponding permeability values of these simulations. For the x- and z-directions, all the results fall in a narrow range with a slightly higher variability in the 6 pixel radius case. On the other hand, the y-direction results show that the permeability obtained using a single slice (K_1) is a fraction of K_{1000} and the ratio increases monotonically as the number of slices increases. However, repeating the same simulations without defining implicit inlet/outlet resulted in elimination of the monotonic increase as seen in Fig. 11c for $r = 10$ pixel case (and in Supporting Fig. 8b and d for $r = 6$ and $r = 14$ pixel cases) where the scatter of y-direction results was comparable with that of other two directions. This confirms that the

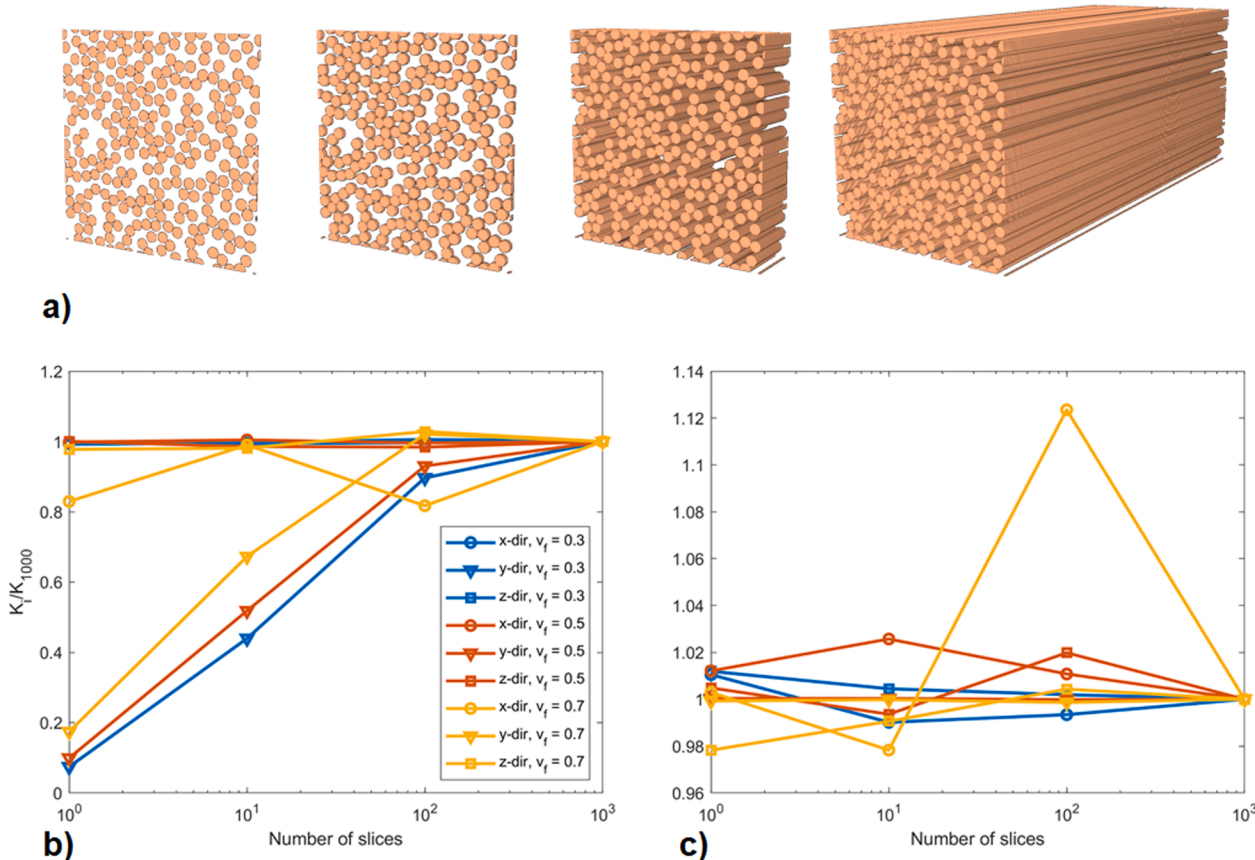


Fig. 11. Influence of 3D image depth on flow simulations. a) An arbitrary microstructure with extrusion depths of 1, 10, 100, and 1000 slices. b) Permeability results normalized with respect to the permeability of images with depth of 1000 (K_i/K_{1000} where $i = 1, 10, 100$, or 1000) for $r = 10$ pixel images when implicit inlet/outlet is used. c) Same results when implicit inlet/outlet is not used in the simulations.

difference between the 2D and 3D results in Fig. 9b originates from the use of implicit inlet/outlet voxels or rather its unsuitability with 2D simulations along y -direction. Based on this conclusion, the further analyses reported herein focus on the predictive capabilities of circuit analogy based extension of neural network predictions along the transverse directions x and z .

3.2.2. Case studies

Based on the previous subsection's results, we analyze two case studies which focus on transverse permeability prediction (*i.e.*, K_x and K_z) in the cases where the input image size differs from what the neural network takes as input, more precisely images with a resolution different from the 400×400 pixel dimensions. In the following subsections, we

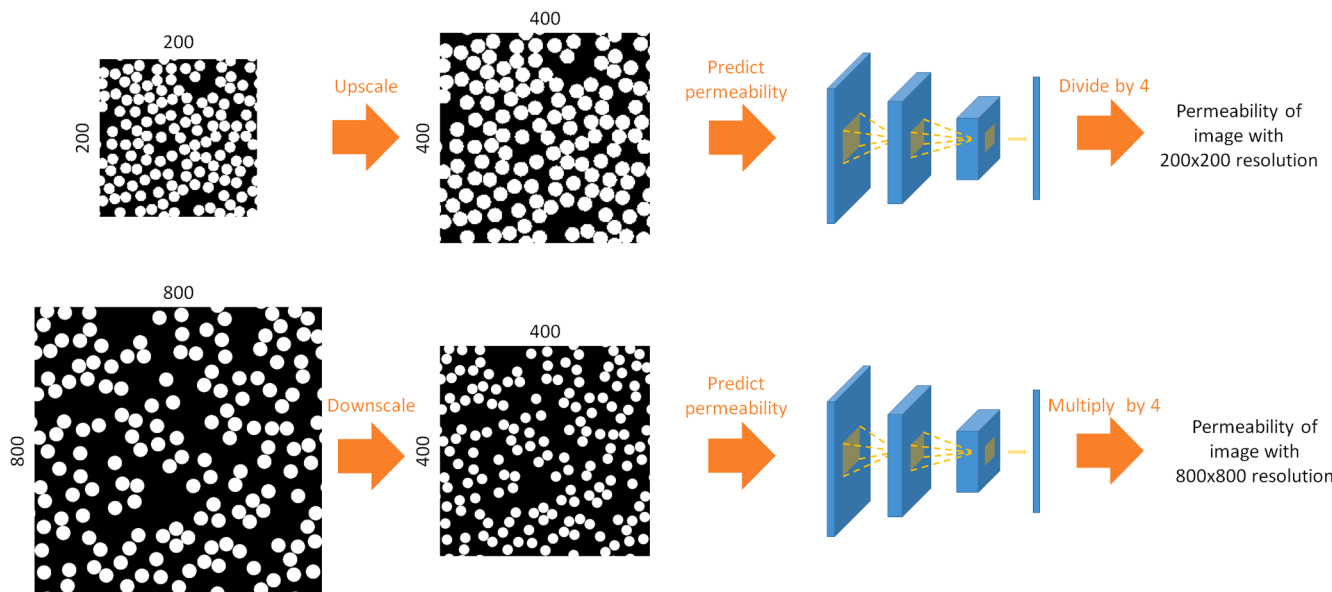


Fig. 12. A visual summary of permeability calculation of images with resolution other than 400×400 pixels. Pictures are not to be scaled.

first investigate the prediction accuracy of the neural network with square images that can have either smaller or larger edge length than 400 pixels and then investigate the prediction accuracy on rectangular images of real microstructures where the fiber radius r as well as v_f in individual slices is variable; for the latter purpose we make use of the dataset distributed within the framework of virtual permeability benchmark study, which consisted of a 3D binary image with dimensions of $1003 \times 124 \times 973$ voxels.

3.2.2.1. Input image with a different size. One limitation of the neural network architecture used in this study is its inflexibility to the input image size. As described in 2.3, our neural network expects a binary image with 400×400 pixel dimensions. However, in practice, one can collect images via different methods such as micrography that not necessarily lead to the aforementioned dimensions. A straightforward route is outlined in Fig. 12 for square images where one can resize the image to the input dimension expected by the network, estimate the permeability and multiply it with the square of the rescaling ratio as permeability is known to scale with r^2 , thus the square of the edge length since r scales with the edge length. In this case, the rescaling ratio equals to the ratio between the edge lengths of the original image and the resized image.

When considering image scaling, a limitation arises from the statistics of the training data, more specifically from the fact that the fibers in the images used in neural network training have a radius r between 6 and 14 pixels. Rescaling operations may result in fiber radii that are either too small or too large, potentially lowering the prediction accuracy. To investigate whether this is the case, we generated 120 individual images with 200×200 pixels where the r was 4, 7, 10 or 14 pixels and v_f was 0.3, 0.5 or 0.7 (10 images per v_f and pixel per radius combination) and images with 800×800 pixels as will be discussed below. Upon scaling up to the desired dimension of 400×400 pixels these fiber radii double; with 10 and 14 pixels the radius becoming 20 and 28 pixels, thus falling out of the radius range considered during neural network training. In such a case one would expect the 4 and 7 pixel radius cases to have comparable accuracy as that of the original test images whose results are reported in Fig. 5a. Fig. 13a shows that this is indeed the case and the permeability predictions for those two cases are scattered around the equality line and similarly for 10 pixel radius cases except for the high v_f range, as also indicated by the purple arrow. Accuracy is significantly lower for $r = 14$ pixel cases that manifests itself across the whole v_f range and amplified at higher v_f values as also indicated by the dashed green line. As speculated above, we suspect that

this behavior originates from the fiber radius ($14 \text{ pixels} \times 2 = 28 \text{ pixels}$) being out of the range of the fiber radius in the training images (6 to 14 pixels), thus the microstructure statistics not being considered during training. We verify this conclusion by exploiting the periodic boundaries of these images and generating 400×400 pixel images by stitching four identical copies of each 200×200 image as depicted in Fig. 14. By this practice, the fiber radii remain untouched; and in this case only the 4 pixel radius falls out of the training range. As seen in Fig. 15, predictions of the 14 pixel images are scattered around the equality line indicating a much better accuracy in comparison to what is reported in Fig. 13a. Similarly, prediction accuracy for the 10 pixel radius images at high v_f range is improved in comparison to their upscaled counterparts reported in Fig. 13a, but an overestimation similar to what is reported in Fig. 5a is still present, indicating that it most likely originates from the neural networks' lower accuracy at permeability values below 10^{-13} m^2 . On the contrary, the 4 pixel radius results with high v_f display a departure from the equality line, as indicated by the orange arrow in Fig. 15, in comparison to Fig. 13a and this re-emphasizes the limitation of the neural network when it comes to predicting the permeability of images that contain fibers whose radii are out of the range considered during the neural network training. However, we note that there are several ways around this limitation, be it rescaling or stitching or cropping (which would also provide a route for assessing the permeability of rectangular images) and there exists an ultimate solution that involves training the neural network with a larger radius range.

Similar trends are present in the case of images with 800×800 pixel dimensions. In this case, we generated 120 individual images where the fiber radius was 8, 20, 40 or 50 pixels and v_f was 0.3, 0.5 or 0.7. The fiber radii are halved upon downscaling the images to 400×400 pixel dimensions and the 20 pixel radius becomes 10 pixels which is in the range of fiber radii used in neural network training while the other three cases (8, 40 or 50 pixel radius) falls out of the training range. This reflects on the prediction accuracy of the neural network for this fiber radius as reported in Fig. 13b. The 50 pixel radius images (which become 25 pixels upon downscaling to 400×400 pixels) exhibit the most deviation from the equality line as also indicated by the dashed green line. The 8 and 40 pixel radius cases have relatively better prediction accuracy, despite them also falling out of the training range. This also indicates the robustness of the neural network to deal with microstructures that are not considered during the training. We also note that the 8 pixel results consist of only two separate clusters instead of three (similarly 4 pixel and 7 pixel cases in Fig. 13a). This originates from the simulation results that return 0 permeability at high v_f .

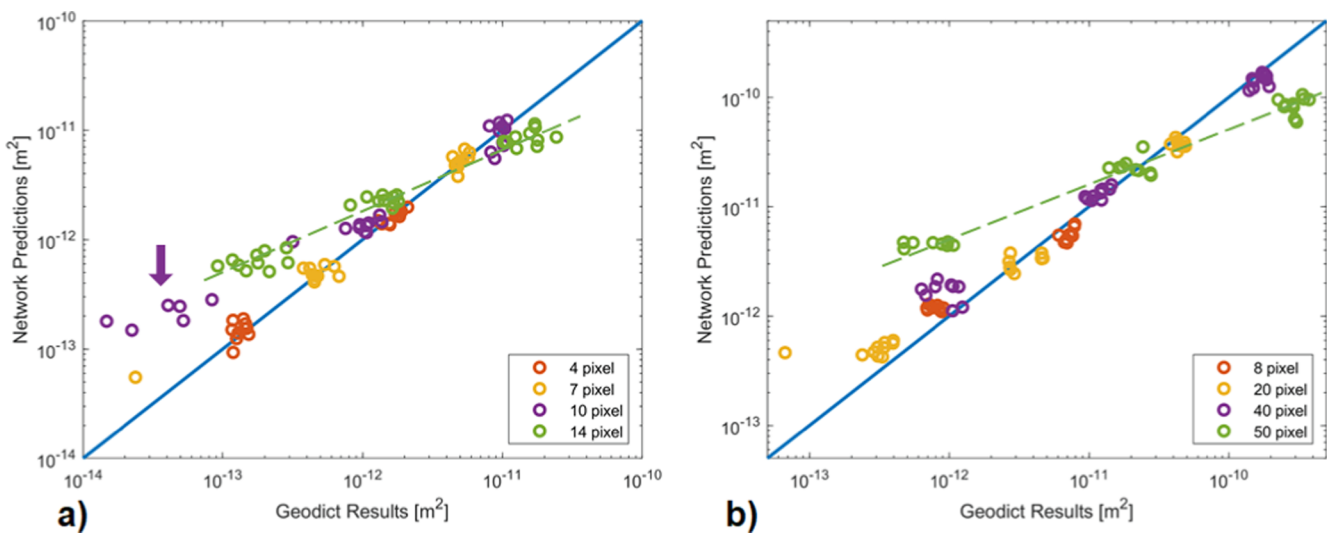


Fig. 13. Predictions for images with resolution other than 400×400 pixels. a) 200×200 pixels, b) 800×800 pixels.

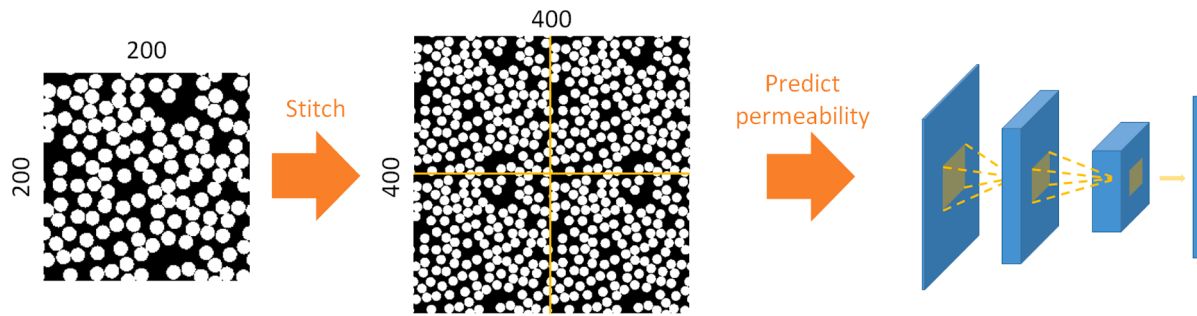


Fig. 14. Permeability calculation of stitched images with 200×200 pixels resolution.

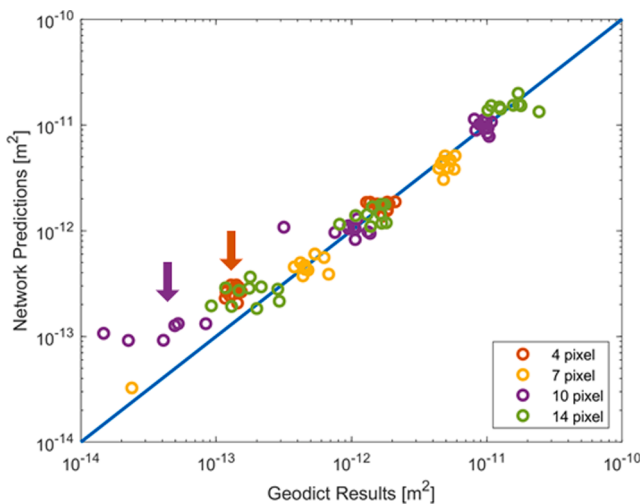


Fig. 15. Predictions for stitched images with resolution of 200×200 pixels.

3.2.2.2. Virtual permeability benchmark dataset. The ultimate test to assess the performance of our network is to subject it to real images (i) that have non-constant fiber radius r and fiber content v_f along the fiber direction, (ii) non-periodic boundary conditions and (iii) that are rectangular in shape with an aspect ratio different from 1. For this purpose, we used the 3D image dataset used in the virtual permeability benchmark whose first results are reported in [83]. The provided binary image has dimensions of $1003 \times 973 \times 124$ voxels and was obtained using X-ray computed microtomography with a carbon fiber yarn and with a spatial resolution of $0.52 \mu\text{m}/\text{voxel}$. Each of the 973 slices along the fiber direction contains several hundreds of fibers whose radii vary between ~ 6 and ~ 12 pixels.

We followed the procedure outlined in Fig. 16 to prepare the images that can be input to the neural network. This consisted in mirroring the image along the z -direction twice to reach dimensions of $1003 \times 973 \times 496$. We then cropped a region from each slice's center with dimensions of 800×400 and this resulted with a 3D image with dimensions of $800 \times 973 \times 400$. We then split this image into two images with the size of $400 \times 973 \times 400$ pixels. We predicted the transverse permeability values (K_x and K_z) of each slice of both parts, then obtained the permeability of each part via circuit analogy of resistances in parallel as also described in subsection 3.1. To estimate the K_x of the complete image ($800 \times 973 \times 400$), we treated the two parts as resistances in series whereas the K_z required treatment of the two image parts as parallel resistances.

Table 2 presents the permeability predictions for both parts of the image as well as the bulk permeability values along the x - and z -directions. Ref [83] reported the K_x estimations of all participants of the virtual permeability benchmark to scatter between $\sim 4 \cdot 10^{-15} \text{ m}^2$ and $\sim 5 \cdot 10^{-13} \text{ m}^2$ with a mean value of $1.06 \cdot 10^{-13} \text{ m}^2$. Considering the large

scatter within the results obtained with the physics-based simulations performed by the participants and the fact that the permeability estimation via our proposed procedure takes less than a minute (most of which is spent for image processing rather than neural network calculations), our estimation of $6.67 \cdot 10^{-14} \text{ m}^2$ can be considered as a very fast and accurate approach for permeability estimation. Another observation in [83] is that the K_z is higher than that in x -direction with a scatter between $\sim 8 \cdot 10^{-15} \text{ m}^2$ and $\sim 7 \cdot 10^{-13} \text{ m}^2$ and a mean value of $1.41 \cdot 10^{-13} \text{ m}^2$. A similar trend is present in our estimations as the K_z is estimated to be $8.79 \cdot 10^{-14} \text{ m}^2$. More interestingly, K_z/K_x ratio in the benchmark results is 1.33 ($1.41 \cdot 10^{-13}/1.06 \cdot 10^{-13}$) while it is 1.32 ($8.79 \cdot 10^{-14}/6.67 \cdot 10^{-14}$) for our predictions. Even though our neural network predictions are only as good as the simulation results that are used for its training, the close match between K_z/K_x values indicates that the network can also be used as a tool to assess the extent of anisotropy in the microstructures.

We note that the extension from 2D to 3D permeability can be further improved by considering the tortuosity induced effects or by altering the operations followed for obtaining the images that can be used as inputs to the neural network. The former can be integrated into the neural network's prediction capability as demonstrated in [84] for simple 2D images. For the latter, we pursued a different strategy to crop and mirror the images as outlined in Supporting Fig. 9. Corresponding permeability predictions in Supporting Table 5 are slightly lower in this case and this is likely to have arisen from the relatively low v_f in the boundaries of the original binary image due to difficulty of circle detection at the image boundaries which was used for obtaining the binary images from the grayscale outputs of microtomography scans.

4. Conclusions

We demonstrated the relevance of a mixed and fast numerical-analytical strategy to estimate the permeability of highly oriented 3D fibrous microstructures, by using permeability estimation of 2D slices with convolutional neural networks (CNNs) and by extending the obtained predictions to full 3D flows via circuit analogy (*i.e.*, simple Voigt and Reuss estimates which are relevant for the considered fibrous microstructures). Despite CNNs being capable of directly predicting the permeability of 3D microstructures, we opted for this mixed strategy to avoid generating and performing flow simulations on thousands of 3D geometries - an operation which would have costed months if not years of CPU time.

We first validated the prediction accuracy of CNN based 2D permeability estimation for transverse and axial permeability values with 400×400 pixel images which contained fibers with radii ranging from 6 pixels to 14 pixels and fiber volume fraction ranging from 0.3 to 0.7. The prediction accuracy was rather high throughout the fiber radius and fiber volume fraction range, with more than 90% of predictions being within $\pm 30\%$ of the simulated results, and also exhibiting a slight decrease at the very low permeability range that might originate from the imbalance in the training data. We then extended the CNN based predictions to estimate the permeability of 3D microstructures by making use of the circuit analogy which called for parallel resistances

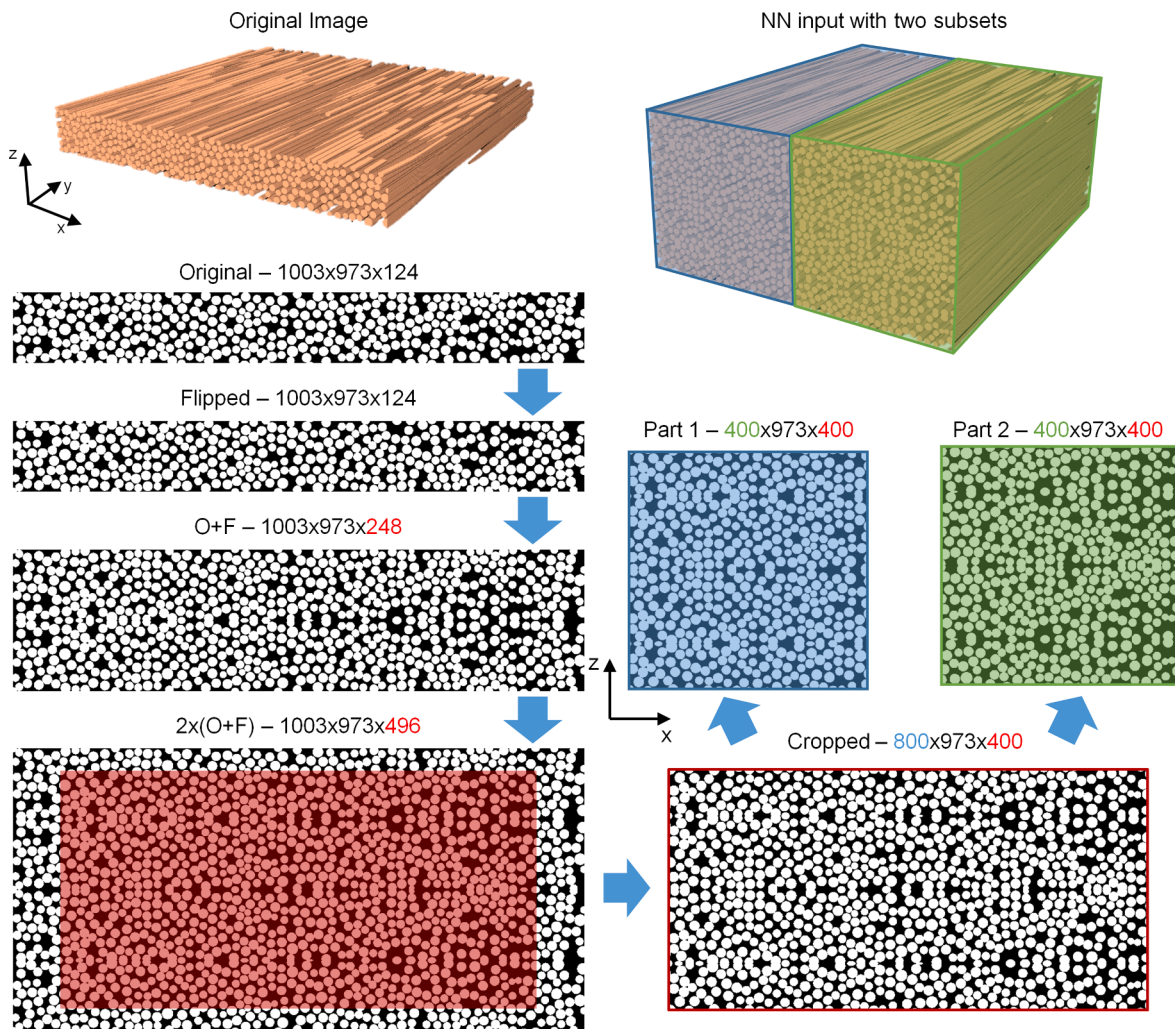


Fig. 16. Summary of the operations carried out to obtain the 3D image used for permeability prediction.

Table 2

Permeability prediction along the x- and z- directions using the CNN trained for transverse permeability prediction. Part 1 and 2 (R_1 and R_2) are constructed as 973 resistors in parallel. Circuit analogy between R_1 and R_2 is constructed as two resistances connected in series for x-direction and as two resistances in parallel for z-direction.

	Part 1	Part 2	Equivalent permeability
Permeability [m^2]	K_x $5.59 \cdot 10^{-14}$	$8.27 \cdot 10^{-14}$	$6.67 \cdot 10^{-14}$
	K_z $7.61 \cdot 10^{-14}$	$9.96 \cdot 10^{-14}$	$8.79 \cdot 10^{-14}$

approach for transverse permeability values (K_x and K_z) and for serial resistances for the longitudinal permeability, K_y . Along the transverse directions, the estimations well fitted the permeability values obtained from fiber scale flow simulations performed with Geodict across the whole studied range. However, the axial permeability predictions were almost an order of magnitude lower than the reference values obtained from Geodict. An investigation of the source of this mismatch showed that the discrepancy originated from the selection of the boundary conditions in the simulations themselves.

As this work's focus was on the feasibility of using CNNs for permeability prediction, we then investigated cases where the image size was different from what the CNNs expected as the input, namely dimensions of 400×400 pixels. Through analyses of images that are both smaller and larger than this size, we could show that rescaling the images and feeding them to the CNNs yielded highly accurate

predictions. The only issue arose when the fiber radius was significantly out of the range of what the CNNs have been trained with, more precisely the range between 6 pixels and 14 pixels. As the last case study, we estimated the permeability of a microtomography scan image that had rectangular shape, non-periodic boundary conditions and contained fibers with moderate varying radii. For this purpose, we used the dataset provided within the framework of the virtual permeability benchmark and we showed that our approach presents a fast and accurate alternative to the flow simulations that were performed by the benchmark participants to collect permeability information.

Further extension of the CNN prediction capabilities is possible, for instance to collect tortuosity information, as well as other structural descriptors, that can be used to enhance the permeability predictions or to account for the dual scale effects that can arise for some textile reinforcements. Extending the fiber radius range in the training data is another change that could extend the capabilities of the CNNs. However, it might be necessary to enlarge the image size in this case and that would also necessitate altering the networks parameters such as padding and filter sizes or adding a new convolutional block to the network.

CRediT authorship contribution statement

Baris Caglar: Conceptualization, Methodology, Investigation, Writing – original draft, Writing – review & editing. **Guillaume Broggi:** Conceptualization, Methodology, Writing – original draft, Writing – review & editing. **Muhammad A. Ali:** Investigation, Writing – review &

editing. **Laurent Orgéas:** Resources, Writing – review & editing, Funding acquisition. **Véronique Michaud:** Conceptualization, Writing – review & editing, Supervision, Funding acquisition.

Declaration of Competing Interest

The authors declare that they have no known competing financial interests or personal relationships that could have appeared to influence the work reported in this paper.

Acknowledgements

This research was financially supported by the Swiss National Science Foundation (SNF-182669). We acknowledge the virtual permeability characterization benchmark organizers for making the dataset available for this work. The 3SR Lab is part of the LabEx Tec 21 (Investissements d'Avenir - grant agreement n°ANR-11-LABX-0030) and the Carnot Institute Polynat (ANR16-CARN0025).

Appendix A. Supplementary material

Supplementary data to this article can be found online at <https://doi.org/10.1016/j.compositesa.2022.106973>.

References

- [1] Michaud V. A Review of Non-saturated Resin Flow in Liquid Composite Moulding processes. *Transp Porous Media* 2016;115(3):581–601.
- [2] Salvatori D, Caglar B, Teixidó H, Michaud V. Permeability and capillary effects in a channel-wise non-crimp fabric. *Compos Part A Appl Sci Manuf* 2018;108:41–52.
- [3] Staal J, Caglar B, Hank T, Wardle BL, Gorbatikh L, Lomov SV, et al. In-series sample methodology for permeability characterization demonstrated on carbon nanotube-grafted alumina textiles. *Compos Part A Appl Sci Manuf* 2021;150:106631.
- [4] Arteiro A, Furtado C, Catalanotti G, Linde P, Camanho PP. Thin-ply polymer composite materials: A review. *Compos A Appl Sci Manuf* 2020;132(105777).
- [5] Advani SG, Sozer EM. Process Modeling in Composites Manufacturing. CRC Press; 2010.
- [6] Lomov SV, Huysmans G, Luo Y, Parnas RS, Prodromou A, Verpoest I, et al. Textile composites: Modelling strategies. *Compos Part A Appl Sci Manuf* 2001;32(10):1379–94.
- [7] Caglar B, Salvatori D, Sozer EM, Michaud V. In-plane permeability distribution mapping of isotropic mats using flow front detection. *Compos Part A Appl Sci Manuf* 2018;113:275–86.
- [8] Sas HS, Simacek P, Advani SG. A methodology to reduce variability during vacuum infusion with optimized design of distribution media. *Compos Part A Appl Sci Manuf* 2015;78:223–33.
- [9] Wang J, Simacek P, Advani SG. Use of Centroidal Voronoi Diagram to find optimal gate locations to minimize mold filling time in resin transfer molding. *Compos Part A Appl Sci Manuf* 2016;87:243–55.
- [10] Arber R, Beraud JM, Binetruy C, Bizet L, Bréard J, Comas-Cardona S, et al. Experimental determination of the permeability of textiles: A benchmark exercise. *Compos Part A Appl Sci Manuf* 2011;42(9):1157–68.
- [11] Vernet N, Ruiz E, Advani S, Alms JB, Aubert M, Barbuski M, et al. Experimental determination of the permeability of engineering textiles: Benchmark II. *Compos Part A Appl Sci Manuf* 2014;61:172–84.
- [12] May D, Aktas A, Advani SG, Berg DC, Endruweit A, Fauster E, et al. In-Plane Permeability Characterization of Engineering Textiles Based On Radial Flow Experiments: A Benchmark Exercise. *Compos Part A Appl Sci Manuf* 2019;121:100–14.
- [13] Yong AXH, Aktas A, May D, Endruweit A, Advani SG, Hubert P, et al. Out-of-plane permeability measurement for reinforcement textiles: A benchmark exercise. *Compos Part A Appl Sci Manuf* 2021;148(106480).
- [14] Michaud V. Permeability properties of composite reinforcements. *Compos Reinf Optim Perform* 2021;443:72.
- [15] Yun M, Sas HS, Simacek P, Advani SG. Characterization of 3D fabric permeability with skew terms. *Compos Part A Appl Sci Manuf* 2017;97:51–9.
- [16] Verleye B, Lomov SV, Long A, Verpoest I, Roose D. Permeability prediction for the meso-macro coupling in the simulation of the impregnation stage of Resin Transfer Moulding. *Compos Part A Appl Sci Manuf* 2010;41(1):29–35.
- [17] Liu HL, Hwang WR. Permeability prediction of fibrous porous media with complex 3D architectures. *Compos Part A Appl Sci Manuf* 2012;43(11):2030–8.
- [18] Zeng X, Endruweit A, Brown LP, Long AC. Numerical prediction of in-plane permeability for multilayer woven fabrics with manufacture-induced deformation. *Compos Part A Appl Sci Manuf* 2015;77:266–74.
- [19] Belov EB, Lomov SV, Verpoest I, Peters T, Roose D, Parnas RS, et al. Modelling of permeability of textile reinforcements: Lattice Boltzmann method. *Compos Sci Technol* 2004;64(7-8):1069–80.
- [20] Daelemans L, Tomme B, Caglar B, Michaud V, Van Stappen J, Cnudde V, et al. Kinematic and mechanical response of dry woven fabrics in through-thickness compression: Virtual fiber modeling with mesh overlay technique and experimental validation. *Compos Sci Technol* 2021;207(108706).
- [21] Swery EE, Meier R, Lomov SV, Drechsler K, Kelly P. Predicting permeability based on flow simulations and textile modelling techniques: Comparison with experimental values and verification of FlowTex solver using Ansys CFX. *J Compos Mater* 2016;50(5):601–15.
- [22] Caglar B, Orgéas L, Rolland du Roscoat S, Sozer EM, Michaud V. Permeability of textile fabrics with spherical inclusions. *Compos Part A Appl Sci Manuf* 2017;99:1–14.
- [23] Straumit I, Hahn C, Winterstein E, Plank B, Lomov SV, Wevers M. Computation of permeability of a non-crimp carbon textile reinforcement based on X-ray computed tomography images. *Compos Part A Appl Sci Manuf* 2016;81:289–95.
- [24] Ghafour TA, Balbinot C, Audry N, Martoia F, Orgéas L, Dumont PJJ, et al. Permeability of flax fibre mats: Numerical and theoretical prediction from 3D X-ray microtomography images. *Compos Part A Appl Sci Manuf* 2021;151:106644.
- [25] Soltani P, Zarrebini M, Laghaei R, Hassanpour A. Prediction of permeability of realistic and virtual layered nonwovens using combined application of X-ray MCT and computer simulation. *Chem Eng Res Des* 2017;124:299–312.
- [26] Ali MA, Umer R, Khan KA, Cantwell WJ. Application of X-ray computed tomography for the virtual permeability prediction of fiber reinforcements for liquid composite molding processes : A review. *Compos Sci Technol* 2019;184:107828.
- [27] Karaki M, Younes R, Troch F, Lafon P. Progress in Experimental and Theoretical Evaluation Methods for Textile Permeability. *Journal of Composites Science* 2019;3(3):73.
- [28] Bear J. Dynamics of fluids in porous media. Courier Corporation; 1988.
- [29] Koponen A, Kandhai D, Hellén E, Alava M, Hoekstra A, Kataja M, et al. Permeability of three-dimensional random fiber webs. *Phys Rev Lett* 1998;80(4):716–9.
- [30] Davies CN. The Separation of Airborne Dust and Particles. *Proc Inst Mech Eng Part B Manag Eng Manuf* 1953;167(1B):185–213.
- [31] Tomadakis MM, Robertson TJ. Viscous permeability of random fiber structures: Comparison of electrical and diffusional estimates with experimental and analytical results. *J Compos Mater* 2005;39(2):163–88.
- [32] Knackstedt MA, Duplessis JP. Simple permeability model for natural granular media. *Geophys Res Lett* 1996;23(13):1609–12.
- [33] Gebart BR. Permeability of unidirectional reinforcements for RTM. *J Compos Mater* 1992;26(8):1100–33.
- [34] Berdichevsky AL, Cai Z. Preform permeability predictions by self-consistent method and finite element simulation. *Polym Compos* 1993;14(2):132–43.
- [35] Cai Z, Berdichevsky AL. An improved self-consistent method for estimating the permeability of a fiber assembly. *Polym Compos* 1993;14(4):314–23.
- [36] Kuwabara S. The forces experienced by randomly distributed parallel circular cylinders or spheres in a viscous flow at small Reynolds numbers. *J Phys Soc Japan* 1959;14(4):527–32.
- [37] Van der Westhuizen J, Prieur Du Plessis J. An attempt to quantify fibre bed permeability utilizing the phase average Navier-Stokes equation. *Compos Part A Appl Sci Manuf* 1996;27(4):263–9.
- [38] Drummond JE, Tahir MI. Laminar viscous flow through regular arrays of parallel solid cylinders. *Int J Multiph Flow* 1984;10(5):515–40.
- [39] Brusche MV, Advani SG. Flow of generalized Newtonian fluids across a periodic array of cylinders. *J Rheol* 1993;37(3):479–98.
- [40] Tamayol A, Bahrami M. Analytical determination of viscous permeability of fibrous porous media. *Int J Heat Mass Transf* 2009;52(9-10):2407–14.
- [41] Tamayol A, Bahrami M. Transverse permeability of fibrous porous media. *Phys Rev E - Stat Nonlinear, Soft Matter Phys* 2011;83:1–9.
- [42] Phelan FR, Wise G. Analysis of transverse flow in aligned fibrous porous media. *Compos Part A Appl Sci Manuf* 1996;27(1):25–34.
- [43] LeCun Y, Bengio Y, Hinton G. Deep learning. *Nature* 2015;521(7553):436–44.
- [44] Zhang Z, Geiger J, Pohjalainen J, Mousa A-D, Jin W, Schuller B, Schuller B. *ACM Trans Intell Syst Technol* 2018;9(5):1–28.
- [45] Yun M-Y, Lopez E, Chinesta F, Advani S. Manifold embedding of heterogeneity in permeability of a woven fabric for optimization of the VARTM process. *Compos Sci Technol* 2018;168:238–45.
- [46] Kuutti S, Bowden R, Jin Y, Barber P, Fallah S. A Survey of Deep Learning Applications to Autonomous Vehicle Control. *IEEE Trans Intell Transp Syst* 2021;22(2):712–33.
- [47] Esteva A, Robicquet A, Ramsundar B, Kuleshov V, DePristo M, Chou K, et al. A guide to deep learning in healthcare. *Nat Med* 2019;25(1):24–9.
- [48] Lu Lu, Dao M, Kumar P, Ramamurti U, Karniadakis GE, Suresh S. Extraction of mechanical properties of materials through deep learning from instrumented indentation. *Proc Natl Acad Sci* 2020;117(13):7052–62.
- [49] Guo K, Yang Z, Yu C-H, Buehler MJ. Artificial intelligence and machine learning in design of mechanical materials. *Mater Horizons* 2021;8(4):1153–72.
- [50] Abueidda DW, Almasri M, Ammourah R, Ravaioli U, Jasiuk IM, Sobh NA. Prediction and optimization of mechanical properties of composites using convolutional neural networks. *Compos Struct* 2019;227:111264.
- [51] Rong Q, Wei H, Huang X, Bao H. Predicting the effective thermal conductivity of composites from cross sections images using deep learning methods. *Compos Sci Technol* 2019;184:1–19.
- [52] Baqué P, Remelli E, Fleuret F. International Conference on Machine Learning 2018: 472–81.
- [53] Jung K, Chang S. Advanced deep learning model-based impact characterization method for composite laminates. *Compos Sci Technol* 2021;207:108713.

- [54] Brunton SL, Noack BR, Koumoutsakos P. Machine Learning for Fluid Mechanics. *Annu Rev Fluid Mech* 2020;52(1):477–508.
- [55] Santos JE, Xu D, Jo H, Landry CJ, Pyrcz MJ. PoreFlow-Net : A 3D convolutional neural network to predict fluid flow through porous media. *Adv Water Resour* 2020;138.
- [56] Wu H, Fang WZ, Kang Q, Tao WQ, Qiao R. Predicting Effective Diffusivity of Porous Media from Images by Deep Learning. *Sci Rep* 2019;9:1–12.
- [57] Araya-Polo M, Alpak FO, Hunter S, Hofmann R, Saxena N. Deep learning–driven permeability estimation from 2D images. *Comput Geosci* 2020;24(2):571–80.
- [58] Da WY, Armstrong RT, Mostaghimi P. Boosting Resolution and Recovering Texture of 2D and 3D Micro-CT Images with Deep Learning. *Water Resour Res* 2020;56:1–21.
- [59] Tembely M, AlSumaiti AM, Alameri WS. Machine and deep learning for estimating the permeability of complex carbonate rock from X-ray micro-computed tomography. *Energy Rep* 2021;7:1460–72.
- [60] Kamrava S, Tahmasebi P, Sahimi M. Linking Morphology of Porous Media to Their Macroscopic Permeability by Deep Learning. *Transp Porous Media* 2020;131(2):427–48.
- [61] Santos JE, Xu D, Jo H, Landry CJ, Prodanović M, Pyrcz MJ. PoreFlow-Net: A 3D convolutional neural network to predict fluid flow through porous media. *Adv Water Resour* 2020;138:103539.
- [62] Gärttner S, Alpak FO, Meier A, Ray N, Frank F. Estimating permeability of 3D micro-CT images by physics-informed CNNs based on DNS. *arXiv preprint arXiv:* 2109.01818. 2021 Sep 4.
- [63] Da WY, Chung T, Armstrong RT, Mostaghimi P. ML - LBM : Predicting and Accelerating Steady State Flow Simulation in Porous Media with Convolutional Neural Networks. *Transp Porous Media* 2021.
- [64] Wu J, Yin X, Xiao H. Seeing permeability from images: fast prediction with convolutional neural networks. *Sci Bull* 2018;63(18):1215–22.
- [65] Rimmel O, May D. Modeling transverse micro flow in dry fiber placement preforms. *J Compos Mater* 2020;54(13):1691–703.
- [66] Chen X, Papathanasiou TD. On the variability of the Kozeny constant for saturated flow across unidirectional disordered fiber arrays. *Compos Part A Appl Sci Manuf* 2006;37(6):836–46.
- [67] Chen X, Papathanasiou T. Micro-scale modeling of axial flow through unidirectional disordered fiber arrays. *Compos Sci Technol* 2007;67(7–8):1286–93.
- [68] Ali MA, Umer R, Khan KA, Cantwell WJ. In-plane virtual permeability characterization of 3D woven fabrics using a hybrid experimental and numerical approach. *Compos Sci Technol* 2019;173:99–109.
- [69] Krizhevsky A, Sutskever I, Hinton GE. ImageNet classification with deep convolutional neural networks. *Commun ACM* 2017;60(6):84–90.
- [70] Alom MZ, Taha TM, Yakopcic C, Westberg S, Sidike P, Nasrin MS, et al. The History Began from AlexNet. A Comprehensive Survey on Deep Learning Approaches 2018.
- [71] Aldahoul N, Htike ZZ. Benchmarking different deep regression models for predicting image rotation angle and robot's end effector's position. 2019 7th Int Conf Mechatronics Eng ICOM. 2019 2019.
- [72] Srivastava N, Hinton G, Krizhevsky A. Dropout: A Simple Way to Prevent Neural Networks from Overfitting. *J Mach Learn Res* 2015;15:1929–58.
- [73] Ioffe S, Szegedy C. Batch normalization: Accelerating deep network training by reducing internal covariate shift. 32nd Int Conf Mach Learn ICML 2015 2015;1:448–56.
- [74] Garbin C, Zhu X, Marques O. Dropout vs. batch normalization: an empirical study of their impact to deep learning. *Multimed Tools Appl* 2020;79(19–20):12777–815.
- [75] Park S, Kwak N. Analysis on the Dropout Effect in Convolutional Neural Networks. In: Lai S-H, Lepetit V, Nishino K, Sato Y, editors. *Comput. Vis. – ACCV 2016*, Cham: Springer International Publishing; 2017, p. 189–204.
- [76] Buda M, Maki A, Mazurowski MA. A systematic study of the class imbalance problem in convolutional neural networks. *Neural Networks* 2018;106:249–59.
- [77] Johnson JM, Khoshgoftaar TM. Survey on deep learning with class imbalance. *J Big Data* 2019;6(1).
- [78] Yang Z, Yabansu YC, Al-Bahrani R, Liao W-K, Choudhary AN, Kalidindi SR, et al. Deep learning approaches for mining structure-property linkages in high contrast composites from simulation datasets. *Comput Mater Sci* 2018;151:278–87.
- [79] Ali MA, Khan KA, Umer R. An electric circuit analogy-based homogenization approach for predicting the effective permeability of complex dual-scale porous media. *Mater Today Commun* 2021;28:102565.
- [80] Endruweit A, Gommer F, Long AC. Stochastic analysis of fibre volume fraction and permeability in fibre bundles with random filament arrangement. *Compos Part A Appl Sci Manuf* 2013;49:109–18.
- [81] Geoffre A, Ghoshin M, Moulin N, Bruchon J, Drapier S. Bounding transverse permeability of fibrous media: a statistical study from random representative volume elements with consideration of fluid slip. *Int J Multiph Flow* 2021;143:103751.
- [82] Saxena N, Mavko G, Hofmann R, Srisutthiyakorn N. Estimating permeability from thin sections without reconstruction: Digital rock study of 3D properties from 2D images. *Comput Geosci* 2017;102:79–99.
- [83] May D, Syerko E, Schmidt T, Binetruy C, da Silva LR, Lomov SV, et al. Benchmarking Virtual Permeability Predictions of Real Fibrous Microstructure. *Proc Am Soc Compos Tech Conf Compos Mater* 2021.
- [84] Graczyk KM, Matyka M. Predicting porosity, permeability, and tortuosity of porous media from images by deep learning. *Sci Rep* 2020;10:1–11.